

ARTICLE

<https://doi.org/10.1038/s42004-019-0227-z>

OPEN

# Understanding charge compensation mechanisms in $\text{Na}_{0.56}\text{Mg}_{0.04}\text{Ni}_{0.19}\text{Mn}_{0.70}\text{O}_2$

Le Anh Ma <sup>1</sup>, Felix Massel <sup>2</sup>, Andrew J. Naylor <sup>1</sup>, Laurent-C. Duda <sup>2</sup> & Reza Younesi <sup>1\*</sup>

Sodium-ion batteries have become a potential alternative to Li-ion batteries due to the abundance of sodium resources. Sodium-ion cathode materials have been widely studied with particular focus on layered oxide lithium analogues. Generally, the capacity is limited by the redox processes of transition metals. Recently, however, the redox participation of oxygen gained a lot of research interest. Here the Mg-doped cathode material  $\text{P2-Na}_{0.56}\text{Mg}_{0.04}\text{Ni}_{0.19}\text{Mn}_{0.70}\text{O}_2$  is studied, which is shown to exhibit a good capacity (ca. 120 mAh/g) and high average operating voltage (ca. 3.5 V vs.  $\text{Na}^+/\text{Na}$ ). Due to the Mg-doping, the material exhibits a reversible phase transition above 4.3 V, which is attractive in terms of lifetime stability. In this study, we combine X-ray photoelectron spectroscopy, X-ray absorption spectroscopy and resonant inelastic X-ray scattering spectroscopy techniques to shed light on both, cationic and anionic contributions towards charge compensation.

<sup>1</sup>Department of Chemistry-Ångström Laboratory, Uppsala University, SE-75121 Uppsala, Sweden. <sup>2</sup>Department of Physics and Astronomy, Uppsala University, SE-75121 Uppsala, Sweden. \*email: [reza.younesi@kemi.uu.se](mailto:reza.younesi@kemi.uu.se)

The increasing use of electronic devices results in a higher demand for energy storage technologies. Rechargeable lithium-ion batteries (LIBs) have become key components in portable electric devices as well as in the automotive industry as a result of their excellent energy and power capability compared with other battery systems. However, there have been concerns about the Li resources which could be exhausted with the increased demand<sup>1</sup>. Therefore, sodium-ion batteries (SIBs) represent a good alternative in terms of cost-effectiveness and sustainability especially when the energy density is not the most important parameter, for example in stationary applications<sup>2</sup>.

Various cathode materials have been proposed for SIBs, mirroring research approaches for LIBs. These can be categorized into three groups: layered oxides, polyanionic frameworks, and prussian blue analogues<sup>3–8</sup>.

The most extensively studied group is layered oxides of  $\text{NaMX}_2$ -type. They consist of stacked sheets of edge sharing  $\text{MO}_6$  octahedra. According to the notation by Delmas et al.<sup>9</sup>, sodium-based layered oxides can be divided into two main types: O3-type and P2-type, which correspond to the arrangement of sodium ions at octahedral (O) and prismatic (P) sites with the appended number illustrating the number of  $\text{MO}_2$  layers per unit cell. It has been reported that P-type materials show better electrochemical performance compared with O3-type compounds, while P2-structures exhibit better performance than P3-types<sup>10</sup>. P2-type  $\text{Na}_x\text{MnO}_2$  is an attractive cathode material due to its naturally abundant elements, cost-effectiveness, environmental compatibility, and its high specific capacity<sup>4,11</sup>. One drawback is the P2-O2 phase transition at voltages above 4.0 V which results in material degradation and hence decreased lifetime<sup>12,13</sup>. The upper cut-off potential may be lowered to avoid this, while another approach is to improve the structural stability by doping with various metals (e.g. Mg, Ni and Fe) to partially substitute Mn<sup>14</sup>. P2- $\text{Na}_{2/3}\text{Ni}_{1/3}\text{Mn}_{2/3}\text{O}_2$  was first introduced by Lu and Dahn in 2001 (ref. 12). Recent studies have shown that magnesium doping is beneficial for Na–Ni–Mn–O systems as  $\text{Na}_{0.67}\text{Ni}_{0.3-x}\text{Mg}_x\text{Mn}_{0.7}\text{O}_2$  ( $x = 0.05, 0.1$ ) shows a more stable rate capability<sup>15</sup>. In comparison to the undoped material, the Mg-doped material undergoes a reversible P2-OP4 transition at high voltages instead<sup>16–19</sup>.

Beside a relatively long history of Na-layered oxide cathode materials incorporating various transition metals (TMs), anionic redox activity in such materials has recently been the subject of much interest when discussing their charge compensation mechanisms<sup>20</sup>. It is now widely known that capacity can correspond to some or all of the redox activity of TMs or oxygen redox/loss<sup>21</sup>. Therefore, anionic chemistry is highly relevant when designing SIB cathodes, since the capacity can be influenced by

oxygen chemistry. Generally, understanding redox processes in charge compensation mechanisms can be complex. For example, the redox chemistry of  $\text{Li}_2\text{MnO}_3$  is still in discussion, since it was assumed to be electrochemically inactive due to the limited oxidation of Mn which already has the oxidation state of 4+. Many reports have claimed that the electrochemical activity of  $\text{Li}_2\text{MnO}_3$  is due to oxygen loss, i.e., the removal of  $\text{Li}_2\text{O}$ <sup>22,23</sup>. Other groups have reported the oxidation of nonaqueous electrolytes, resulting in generated  $\text{H}^+$  as an exchange for  $\text{Li}^+$ <sup>24–27</sup>. Nevertheless, the electrochemical activation during the first delithiation cycles of  $\text{Li}_2\text{MnO}_3$  and other Li-rich materials are not fully understood and still under investigation<sup>21,24,25,27,28</sup>.

Here we report on the material P2- $\text{Na}_{0.56}\text{Mg}_{0.04}\text{Ni}_{0.19}\text{Mn}_{0.7}\text{O}_2$ , providing complementary insight into the electrochemical redox processes and the structural evolution by a combination of synchrotron energy-tuned (hard X-ray) photoelectron spectroscopy (PES), X-ray absorption spectroscopy (XAS) and resonant inelastic X-ray scattering (RIXS). Building upon previous work by Singh et al.<sup>15</sup>, we could observe not only redox activity of Ni, but also Mn redox activity in our material. Furthermore, we could show via RIXS an enhanced participation of oxygen during the charge compensation processes.

## Results

**Material characterization.** The elemental ratio of the pristine cathode material measured by inductively coupled plasma atomic emission spectroscopy (ICP-OES) showed the composition of  $\text{Na}_{0.56}\text{Mg}_{0.04}\text{Ni}_{0.19}\text{Mn}_{0.7}\text{O}_2$  (normalized to Mn) for the synthesized powder, see Supplementary Table 1. The powder X-ray diffraction (PXRD) results are discussed in Supplementary Note 1; relevant data are shown in Supplementary Table 2 and Supplementary Fig. 1<sup>29–31</sup>.

**Electrochemical performance.** Figure 1a shows galvanostatic cycling of the cathode material  $\text{Na}_{0.56}\text{Mg}_{0.04}\text{Ni}_{0.19}\text{Mn}_{0.7}\text{O}_2$  in a half-cell in the voltage range of 2.0–4.5 V using electrolyte of 1 M  $\text{NaPF}_6$  in PC at 0.1 C rate (i.e. charge/discharge for 10 h). During the first desodiation cycle three plateaus at  $\sim 3.4$ ,  $\sim 3.8$  and  $\sim 4.3$  V can be observed, which is in agreement with previously published results on similar cathode materials,  $\text{Na}_{2/3}\text{Mg}_{0.05}\text{Ni}_{0.25}\text{Mn}_{0.7}\text{O}_2$  and  $\text{Na}_{2/3}\text{Ni}_{1/3}\text{Mn}_{2/3}\text{O}_2$ <sup>13,15</sup>. The electrochemical curves look similar for the first and the following cycles, though some minor capacity loss is detected from the first to the second cycle. In the first desodiation, a capacity of 136 mAh/g corresponds to 0.41  $\text{Na}^+$  was obtained while in the following cycles, the charge capacity drops to a lower value of around 128 mAh/g. Such capacity losses during the first charging cycle have been observed in similar

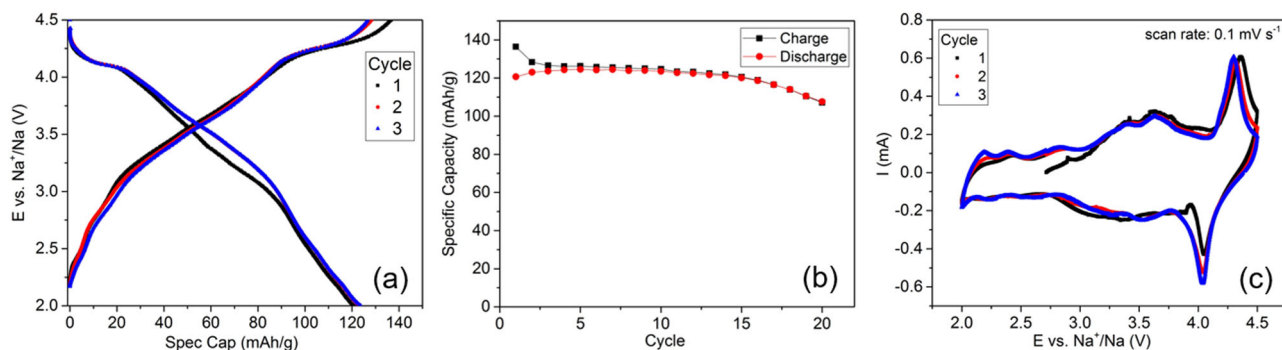


**Fig. 1** Electrochemical performance study.  $\text{Na}_{0.56}\text{Mg}_{0.04}\text{Ni}_{0.19}\text{Mn}_{0.7}\text{O}_2$  in Na half-cells using 1 M  $\text{NaPF}_6$  in PC electrolyte. **a** Galvanostatic cycling at 0.1 C rate during the first three cycles with irreversible capacity loss in the first charging cycle. **b** Galvanostatic cycling at 0.1 C rate for 20 cycles with corresponding specific capacities. **c** Cyclic voltammetry in a voltage window of 2.0–4.5 V at a scan rate of 0.1 mV/s

cathode materials, such as  $\text{Na}_{0.78}\text{Ni}_{0.23}\text{Mn}_{0.69}\text{O}_2$  and have been attributed to anionic contributions<sup>15</sup>. We also tested the cathode material using a different electrolyte of 1 M  $\text{NaPF}_6$  in EC:DEC, which showed similar results; see Supplementary Fig. 2. The galvanostatic cycling curves in Fig. 1 are different from galvanostatic cycling curves shown by Singh et al. where a major change in the potential curve from the first to the second cycle was observed<sup>15</sup>.

In Fig. 1b, the cyclic voltammetry (CV) measurements show at least three regions with redox reactions: (i) between 2.1 and 2.5 V which likely corresponds to  $\text{Mn}^{3+}/\text{Mn}^{4+}$  redox processes, (ii) in the range of 3.1–3.8 V which is most likely due the  $\text{Ni}^{2+}/\text{Ni}^{4+}$  redox reaction, (iii) and at potentials higher than 4.0 V where the peaks can be due to phase transitions, electrolyte decomposition or other processes such as oxygen oxidation observed in previous studies<sup>32–35</sup>. Differential capacity plots (dQ/dV) corroborate observations from CV measurements (see Supplementary Fig. 3). In order to verify which phase transition occurs at voltages higher than 4.0 V, in situ XRD was performed on the material.

**Phase transitions.** The structural evolution in  $\text{P2-Na}_{2/3}\text{Ni}_{1/3}\text{Mn}_{2/3}\text{O}_2$  has previously been studied during desodiation and sodiation<sup>12</sup>. Phase transitions from P2 to O2 have been observed when reaching above 4.3 V. The O2 phase is not favourable since it causes irreversible capacity fading in the first cycles. However, for the Mg-doped  $\text{P2-Na}_{0.56}\text{Mg}_{0.04}\text{Ni}_{0.19}\text{Mn}_{0.70}\text{O}_2$ , an additional peak could be seen in the in situ XRD patterns corresponding to a new and reversible phase which has been reported as the OP4 phase<sup>15</sup>. Similar to that, our tested material  $\text{P2-Na}_{0.56}\text{Mg}_{0.04}\text{Ni}_{0.19}\text{Mn}_{0.70}\text{O}_2$  also exhibits an OP4 peak in the diffraction patterns at  $\sim 17^\circ$  when desodiating above 4.3 V (Fig. 2), in good agreement

with CV measurements showing the potential phase transition at higher voltages. In the second and third cycles (Fig. 2b, c), the 002 reflection peak at  $15.7^\circ$  is still maintained while the new OP4 phase is formed indicating that the new OP4 is not only formed in the first cycle (Fig. 2a), and demonstrating the reversibility of the phase transition. The coexisting phases (P2 and OP4) can be the cause for the irreversible capacity loss during the first cycle. In the following two cycles, the 002 reflection disappears at 4.5 V illustrating a complete and irreversible OP4 phase formation.

**Redox mechanism.** As the stoichiometry analysis shows, the material discussed in this study shows a slight TM deficiency. In order to analyse the role of the TM and oxygen in  $\text{Na}_{0.56}\text{Mg}_{0.04}\text{Ni}_{0.19}\text{Mn}_{0.70}\text{O}_2$ , we performed XAS, RIXS and energy-tuned X-ray PES. XAS is measured using total electron yield (TEY) and total fluorescence yield (TFY). The TEY measurements are more surface sensitive and can probe depths of ca. 2 nm, whereas FY is more bulk sensitive and can measure depths of approximately 100 nm<sup>36–39</sup> (Fig. 3b). For PES, photon energies of 1090, 2350 and 7050 eV were used, which correspond to a depth of analysis at 10, 17 and 50 nm, respectively. The depth of analysis was determined based on the inelastic mean free path  $\lambda$  (IMPF) of polyethylene<sup>40,41</sup>. For the following analysis, samples with different states of charge and numbers of cycles were investigated, as shown in Fig. 3a: a pristine electrode, a sample charged to 3.5 V (1-Ch: 3.5 V), a sample charged to 4.3 V (1-Ch: 4.3 V), a sample charged to 4.5 V (1-Ch: 4.5 V), a sample then discharged to 2.0 V (1-D: 2.0 V) and a sample charged to 4.5 V in the second cycle (2-Ch: 4.5 V). For the discharging and charging processes, equivalent terms such as sodiation and desodiation are used, respectively.

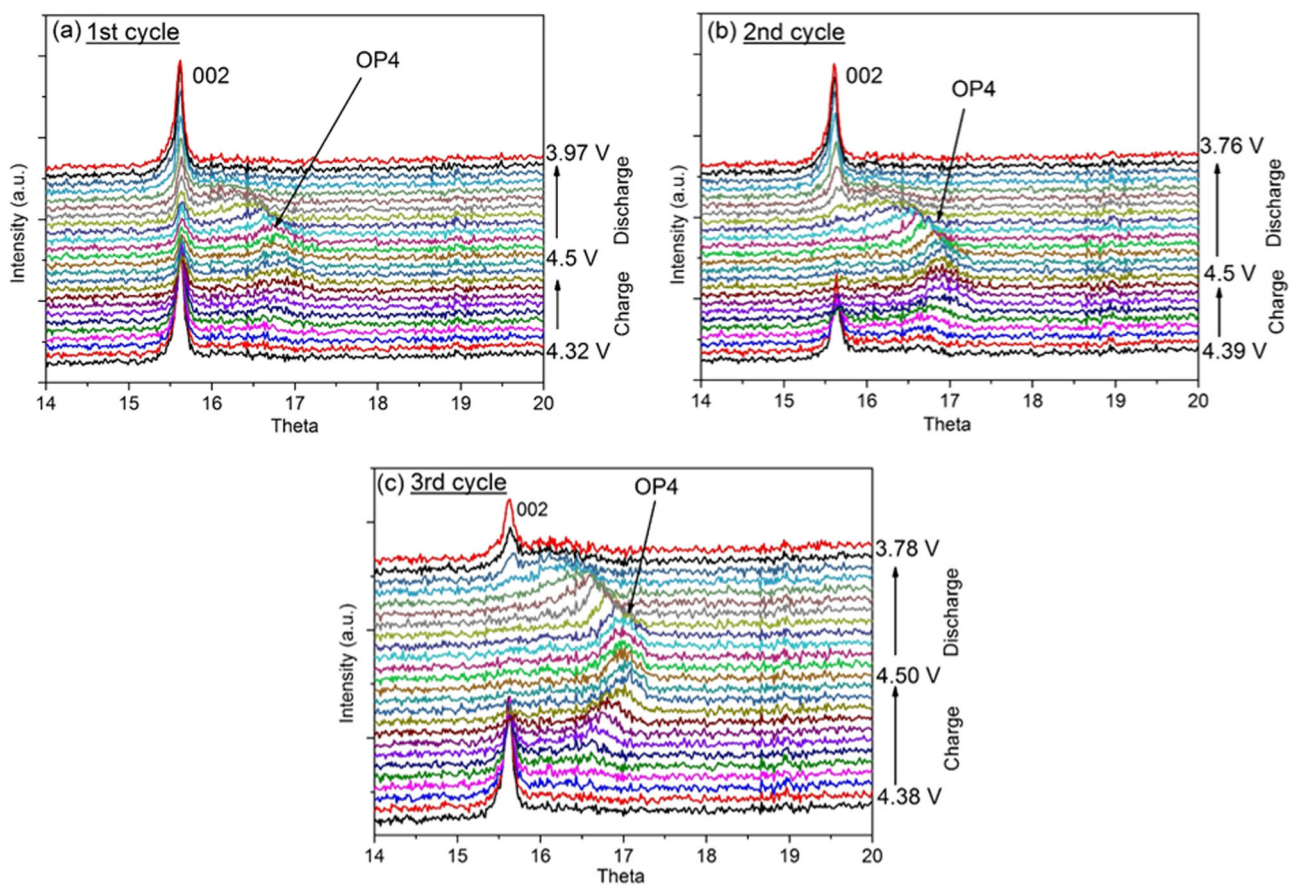


**Fig. 2** In situ XRD patterns of  $\text{Na}_{0.56}\text{Mg}_{0.04}\text{Ni}_{0.19}\text{Mn}_{0.70}\text{O}_2$  galvanostatically cycled. Cells have been cycled using electrolyte of 1 M  $\text{NaPF}_6$  in PC at a rate of 15 mA/g. Measured XRD pattern during **a** the first cycle, **b** the second cycle and **c** the third cycle

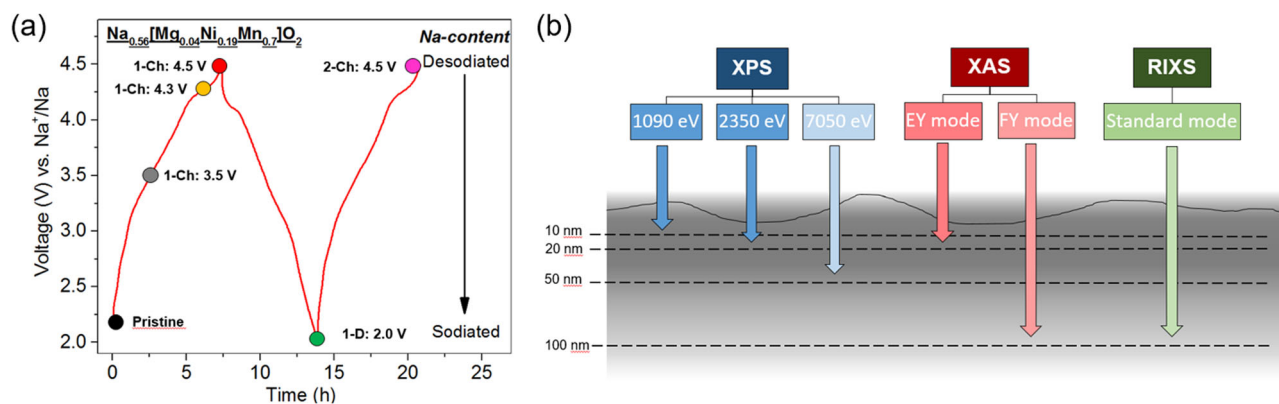


**Fig. 3** Sample analysis. **a**  $\text{Na}_{0.56}\text{Mg}_{0.04}\text{Ni}_{0.19}\text{Mn}_{0.70}\text{O}_2$  cycled at 0.1 C rate to certain states of charge in the first two cycles for XAS, RIXS and PES analysis. **b** Schematic of the techniques used with corresponding depths of analysis

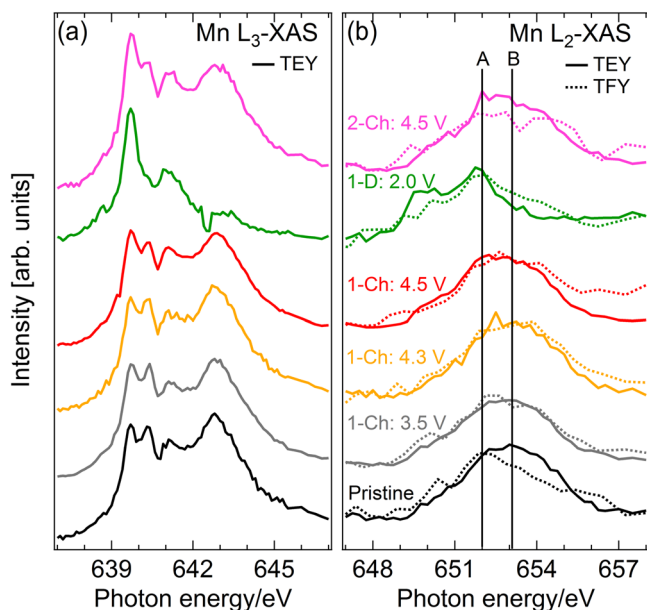


**Fig. 4** X-ray absorption spectroscopy results of Mn L-edge. Spectra measured at **a** TEY signal of  $L_3$ -edge and **b** TEY (solid) and TFY (dashed) signal of  $L_2$ -edge

Figure 4 shows the evolution of the absorption spectra over the Mn L-edge. Panels a and b show the  $L_3$  and  $L_2$ -edge spectra, respectively. In  $\text{Na}_{0.56}\text{Mg}_{0.04}\text{Ni}_{0.19}\text{Mn}_{0.70}\text{O}_2$ , both Mn and Ni are in an octahedral local site symmetry surrounded by six oxygen anions. TM L-edge absorption profiles share certain key features across differing crystal structures as long as they have similar local site symmetry. This makes it possible to compare spectral profiles with those of compounds with known oxidation state and thus draw conclusions about the present oxidation distribution<sup>42</sup>. The surface-related TEY spectrum of the pristine sample exhibits strong spectral fingerprints of  $\text{Mn}^{4+}$  with its typical double feature structure at 640.3 and 642.8 eV as well as an admixture contribution of  $\text{Mn}^{2+}$  with a strong feature at 639.7 eV and a weaker feature at 641.1 eV (ref. 42), which means that the surface of the pristine material shows predominantly  $\text{Mn}^{4+}$  oxidation with a smaller portion being  $\text{Mn}^{2+}$ . Throughout the whole desodiation process to 1-Ch: 4.5 V the spectral shapes show minor changes, indicating that the surface Mn is not active in charge compensation during this part of the cycle. Conversely, upon resodiation to 1-D: 2.0 V the spectrum changes dramatically to only exhibit an  $\text{Mn}^{2+}$  signature. Subsequent desodiation in the

second cycle to 2-Ch: 4.5 V shows a return of the  $\text{Mn}^{4+}$  signature with a slightly higher  $\text{Mn}^{2+}$  contribution than observed over the first cycle.

The bulk-sensitive TFY signal is not presented here because the differential-fluorescence-yield effect at the Mn  $L_3$ -edge strongly distorts the spectrum<sup>43,44</sup>. Instead, we can utilize the TFY at the  $L_2$ -edge, which is depicted as dashed traces in Fig. 4b. Though the shorter  $2p_{1/2}$  core hole lifetime broadens the spectrum, making the determination of the oxidation state more difficult, we can draw some conclusion by the shift of the peak centroid<sup>45</sup>. Overall, the bulk-sensitive TFY  $L_2$ -spectra follows the behaviour of the TEY  $L_2$ -spectra. However, one striking difference is seen in the pristine spectrum with a centroid at a lower energy marked by a vertical line labelled A. This line also coincides with the centroid of the resodiated sample spectrum 1-D: 2.0 V, suggesting that the bulk material starts out with a Mn oxidation state dominated by  $\text{Mn}^{2+}$  while its surface is strongly  $\text{Mn}^{4+}$ . Upon charging, the bulk rapidly (already at 3.5 V) attains a similar oxidation state as the surface, i.e. a mixed  $\text{Mn}^{2+/4+}$  mixed oxidation state. Already upon desodiation to 1-Ch: 3.5 V the peak centroid shifts by 1.1 eV towards higher energies (line B).

In summary, we find that while the surface of the pristine material is in a mixed  $\text{Mn}^{2+/4+}$  oxidation state, the bulk is dominated by an  $\text{Mn}^{2+}$  oxidation state that rapidly is oxidized by the initial desodiation to a mixed  $\text{Mn}^{2+/4+}$  oxidation state. We observe that the first resodiation reduces both the surface and the bulk Mn ions to a  $\text{Mn}^{2+}$  oxidation state. At the end of the second desodiation, both the surface and the bulk Mn ions return to their mixed  $2+/4+$  oxidation state. This indicates that both the surface and the bulk Mn ions are active in the charge compensation of the sodiation cycle, whereby the first desodiation seems to have an activation effect on the surface Mn ions.

With Mn 3s spectra in PES, different oxidation states of manganese can be distinguished by the degree of the multiplet splitting (MS). Typically, the relationship between the MS and the oxidation is linear and has been widely discussed in previous reports<sup>46–48</sup>. Hence, with the MS gap energy the oxidation of Mn can be predicted. A gap energy of about 5.9 eV indicates  $\text{Mn}^{2+}$ , 5.5 eV  $\text{Mn}^{3+}$  and 4.8 eV  $\text{Mn}^{4+}$  characteristics. In this respect, Mn 3s spectra can illustrate the trend in oxidation states during desodiation/sodiation. Figure 5a shows Mn 3s spectra measured using an excitation energy of 2350 eV. For the two samples desodiated up to 4.5 V, the gap energy between the two peaks vary from 4.6 to 4.9 eV which is approximately the energy difference expected for  $\text{Mn}^{4+}$ . Thus,  $\text{Mn}^{4+}$  is mainly present in the desodiated samples. After one whole cycle ending with a resodiated state, the energy gap between the two peaks in the Mn 3s spectra increases to 5.7 eV resulting in energy gap values



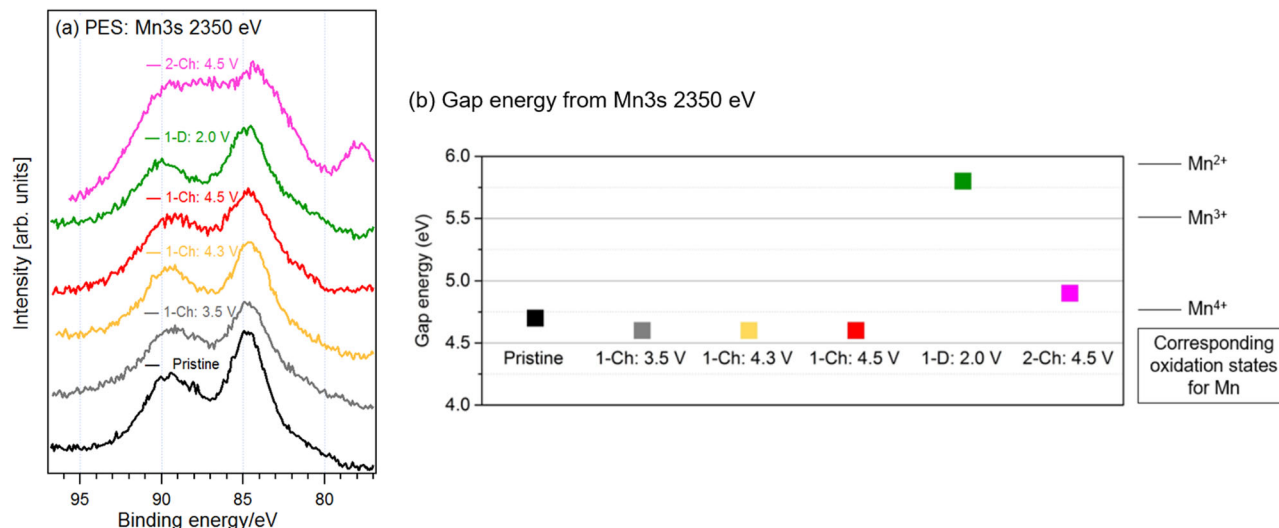


**Fig. 5** X-ray photoelectron spectroscopy results of Mn 3s. **a** PES spectra of Mn3s at 2350 eV and **b** with corresponding gap energies to identify the oxidation state<sup>49</sup>

between those for Mn<sup>3+</sup> and Mn<sup>2+</sup> (ref. 49). Hence, during sodiation Mn undergoes a reduction to lower oxidation states and when desodiated again to higher oxidation states. Therefore, the Mn 3s spectra also indicate a redox activity of manganese during the sodiation and desodiation process which is in good agreement with the XAS measurements.

Sodiation evolution of the Ni L<sub>3</sub>- and L<sub>2</sub>-edge XAS spectra are shown in Supplementary Fig. 4a, b, respectively. Both, surface-sensitive TEY and bulk-sensitive TFY, signals show little change throughout the first cycle. The surface Ni ions remain in an oxidation state of Ni<sup>2+</sup> throughout the first cycle and the second desodiation, which is indicated by the spectral shape of the L<sub>3</sub>-peak<sup>50</sup>. The bulk-sensitive TFY signal is weak and we can only draw firm conclusions about the pristine material, which is predominantly Ni<sup>2+</sup>. On the other hand, there is evidence for oxidation to ~Ni<sup>3+</sup> in the desodiated state of the second cycle 2-Ch: 4.5 V.

The Ni 2p core was studied with soft X-ray and hard X-ray PES (SOXPES and HAXPES) at different photon energies, but no conclusion could be drawn (see Supplementary Fig. 5).

While previous studies have shown that Ni undergoes redox reactions upon desodiation, our results show no Ni redox activity on the surface. However, as for Mn, we cannot exclude the possibility that Ni undergoes redox reactions in the bulk material.

In summary, neither Mn nor Ni undergo oxidation state changes on the surface upon the first desodiation cycle, which could be due to electrolyte decomposition on the electrode surface, especially at these high voltages of 4.5 V. The PES O1s spectra (see Supplementary Fig. 6) show intense peaks associated with carbonate species during desodiation and sodiation processes, which correspond to electrolyte decomposition products. Thus, one can assume that the charge, which is designated for redox processes at the surface, is utilized for the electrolyte decomposition. However, bulk Mn is oxidized during the first desodiation, whereas no statement about bulk Ni can be made due to weak signals. When resodiated subsequently, Mn becomes activated and is fully reduced to Mn<sup>2+</sup> both on the surface and in bulk. When desodiating for the second time, bulk Mn and Ni undergo oxidation. Hence, one can assume that bulk Ni is oxidized in the first desodiation cycle as well as reported before<sup>15</sup>. In contrast to that, surface Mn becomes oxidized to Mn<sup>4+</sup> whereas surface Ni remains unchanged.

XAS was measured on all samples over the O K-edge. At this edge, O 1s core electrons are excited into unoccupied states above the Fermi level. Figure 6a, b shows the surface-sensitive TEY signal and the bulk-sensitive TFY as well as PFY signals, respectively. The pre-edge region spanning from 528.5 to 533.0 eV is associated with O 2p orbitals hybridized mainly with surrounding TM 3d orbitals<sup>51</sup>. We observe a gradual increase of surface hole states during the first desodiation (bottom four spectra in Fig. 6a). Resodiation leads to a complete filling of the low-energy peak that is recovered upon second desodiation. This parallels the evolution observed for Mn.

The bulk O hole state evolution is seen in Fig. 6b (TFY and PFY). Here we only observe small variance in the spectral shape, which at first inspection seems to suggest a weak participation of bulk oxygen states in the charge compensation. However, Fig. 6c shows an analysis of the evolution of the O hole state number. We integrated the recorded pre-edge intensity of TFY and PFY, respectively, at all charge states and normalize it to that of the pristine material. We find that both the surface- and bulk-sensitive signals exhibit similar trend, namely that there is an increase of holes during desodiation and a decrease of holes during resodiation.

To get further insight into the nature of the O hole states, we present O K-edge RIXS maps with incident photon energies over the pre-edge region in Supplementary Fig. 7. The RIXS maps reveal no occurrence of strong localized states, instead we interpret this as the evolution of the valence band with O 2p character. Figure 7 shows the charge evolution of 1D-RIXS spectra at an incident energy of 531.0 eV. The two vertical arrows show the development of a low-energy signature at the end of the first desodiation. This peak disappears upon resodiation and reappears again at second desodiation. This is similar to the observation in a number of Li-rich materials<sup>52</sup> as well as the Na-compound Na<sub>2/3</sub>Mg<sub>0.28</sub>Mn<sub>0.72</sub>O<sub>2</sub><sup>53</sup>. In contrast, we do not observe a strong simultaneous increase of the elastic peak, whose origin is localized oxygen species that undergo a reversible anionic redox process. This may indicate that the emerging feature is related to more delocalized O 2p states corresponding to a more enhanced oxygen hybridization.

Furthermore, we can compare the RIXS spectra of the pristine material (black trace) with the resodiated material (green trace) to

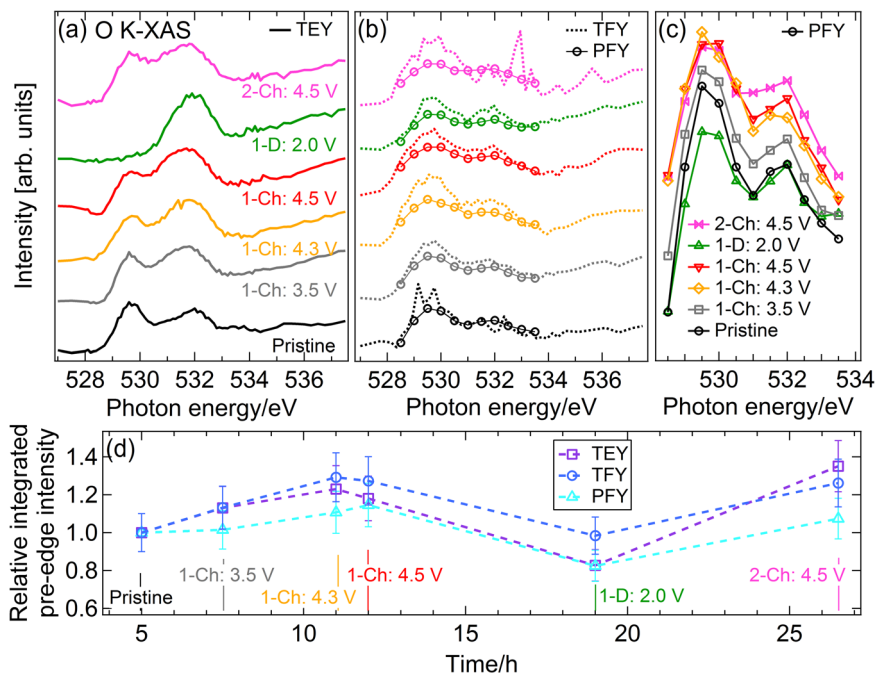


**Fig. 6** XAS spectra of the O K-edge of samples at different sodiation states. Spectra shown in **a** TEY mode and **b** TFY (dashed lines) and PFY (circles) modes. The latter are extracted from the RIXS measurements via integration over the resonant O peak. **c** Superimposed PFY mode spectra. **d** Integration of intensities across the pre-edge (528.5 to 533.0 eV) of all three modes plotted relative to the integrated pre-edge intensity of the respective pristine spectrum. Error bars are  $\pm 10\%$  of the respective value, which has been estimated by evaluating the pre-edge intensities for normalizations to five different points around the normalization point of the presented TEY spectrum of the pristine sample and thus accounting for variations due to its noise level

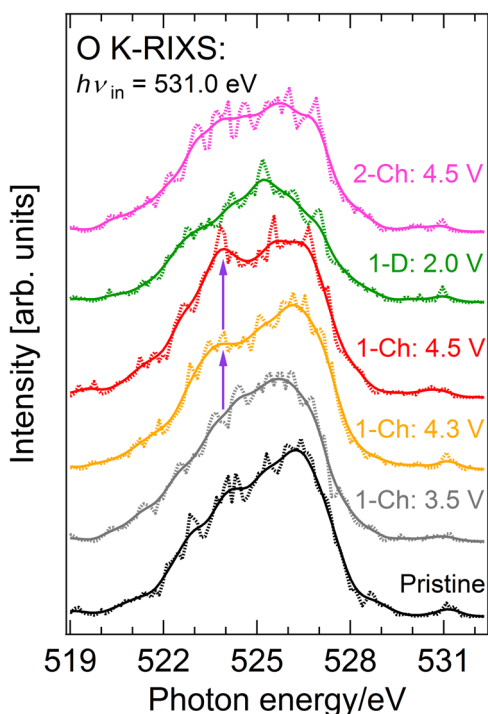


**Fig. 7** RIXS spectrum at an incident photon energy of 531.0 eV. Evolution over the whole sodiation cycle; as guide for the eye, the dashed data traces are overlaid by level 2 binomially smoothed solid traces. The emergence of a peak at 523 eV originating from an O 2p valence band emission is highlighted

get an indication of the degree of reversibility of the charge process. We find that the spectral weight is more symmetric in the resodiated material than in the pristine material, which corroborates that initial activation processes also affect the bulk oxygen ions.

To summarize our observations from the O K-edge, we find evidence for charge compensation of oxygen that is partially reversible. However, bulk oxygen ions also participate in an activation process in the first desodiation.

## Discussion

Consolidating results from both XAS and PES measurements for Mn, Ni and O, we can discuss and summarize the redox reactions occurring in the material, as presented in Fig. 8. During the first desodiation bulk  $\text{Mn}^{2+}$  becomes oxidized to  $\text{Mn}^{4+}$  and surface  $\text{Mn}^{4+}$  remains mostly unchanged in the first desodiation cycle. Surface Ni does not appear to change throughout the cycling. It has been commonly reported that during desodiation, the TMs undergo oxidation in order to balance the charge<sup>15,54</sup>. Therefore Ni is assumed to be consistent with previous results of TM oxidation<sup>15</sup>. During sodiation, both surface and bulk Mn becomes redox activated with  $\text{Mn}^{4+}$  being reduced to  $\text{Mn}^{2+}$ . On desodiation (charge) in the second cycle, surface  $\text{Ni}^{2+}$  remains unchanged but bulk  $\text{Ni}^{2+}$  is oxidized to  $\text{Ni}^{3+}$  while  $\text{Mn}^{2+}$  is partially oxidized to  $\text{Mn}^{4+}$ . Thus, bulk TMs become oxidized during desodiation processes, whereas surface TMs remain unchanged during the first desodiation cycle due to formation of electrolyte decomposition products. However, when desodiating on the second cycle, TMs become partially activated on the surface and in bulk in order to participate in redox processes.

Building on previous studies, RIXS results give additional information on the O K-edge indicating rearrangement of the O 2p band, suggesting a change in electronegativity of the oxygen

	Pristine			Desodiated			Sodiated			Desodiated (2nd)		
Surface	Ni <sup>2+</sup>	Mn <sup>4+</sup>	O parallel to TMs	Ni <sup>2+</sup>	Mn <sup>4+</sup>	O parallel to TMs	Ni <sup>2+</sup>	Mn <sup>2+</sup>	O parallel to TMs	Ni <sup>2+</sup>	Mn <sup>4+</sup>	O parallel to TMs
	Mn <sup>4+</sup>			Mn <sup>4+</sup>			Mn <sup>2+</sup>			Mn <sup>4+</sup>		
Bulk	Ni <sup>2+</sup>	Mn <sup>2+</sup>	O parallel to TMs		Mn <sup>4+</sup>	O parallel to TMs	Ni <sup>2+</sup>	Mn <sup>2+</sup>	O parallel to TMs	Ni <sup>3+</sup>	Mn <sup>4+</sup>	O parallel to TMs
	O <sup>l</sup>			O <sup>m</sup>			O <sup>n</sup>			O <sup>m</sup>		

XAS  
 PES  
 RIXS

= no information

*l ≠ m ≠ n*

**Fig. 8** Summary of oxidation states of Ni, Mn and O according to XAS, RIXS and PES results. Darker shaded colours represent surface-related results (<20 nm depth), whereas lighter shaded colours correspond to bulk related results (50–100 nm depth)

anion<sup>55</sup>. The difference in the electronic character in oxygen are labelled as O<sup>l</sup>, O<sup>m</sup> and O<sup>n</sup>. Although the pristine and the sodiated sample in the first cycle are expected to be the same oxidation state, they are labelled with “l” and “n” emphasizing their different electronic distribution around the oxygen site according to their variance in shape of the RIXS spectra.

In conclusion, redox processes in P2-Na<sub>0.56</sub>Mg<sub>0.04</sub>Ni<sub>0.19</sub>Mn<sub>0.70</sub>O<sub>2</sub> have been studied in detail with PES, XAS and RIXS, demonstrating lattice oxygen redox activity and TM redox processes. It has been verified that the charge compensation during the first Na-extraction occurs via irreversible lattice oxygen rearrangement or loss and a contribution of Mn and Ni oxidation. According to RIXS measurements, the electronic structure of O has been readjusted, which could also be the cause of the capacity loss during the first cycle. Similar to previous work, the charge compensation during the first Na-removal involves Ni- and Mn-redox processes. Our results show redox activities of the TMs only in bulk due to electrolyte decomposition reactions on the surface. Nevertheless, we demonstrate oxygen redox activity during desodiation. In the subsequent sodiation cycle, the material becomes electrochemically activated in both surface and bulk and hence Mn<sup>4+</sup> becomes fully reduced to Mn<sup>2+</sup> serving as a charge compensation mechanism besides participation from oxygen according to RIXS. When the cathode is desodiated during the second charge, both Mn<sup>2+</sup> and Ni<sup>2+</sup> become oxidized to mainly Mn<sup>4+</sup> and Ni<sup>3+</sup> as a charge balance to Na-removal. Electrochemical activation combined with oxygen redox has also been seen, for example, in Li-rich cathode materials<sup>25,27</sup>, suggesting that the present material undergoes similar phenomena. While the exact role of oxygen in this material cannot be assigned as oxygen redox, we have demonstrated an electronic rearrangement of oxygen upon cycling. Generally, the presented results are not only in agreement with previous work, but also enhance the understanding of redox reactions and charge compensation mechanisms for this material with new insights on the oxygen contribution.

## Methods

**Material preparation.** Na<sub>0.56</sub>Ni<sub>0.19</sub>Mg<sub>0.04</sub>Mn<sub>0.7</sub>O<sub>2</sub> was prepared via solid-state reaction of Na<sub>2</sub>CO<sub>3</sub>, NiO, Mn<sub>2</sub>O<sub>3</sub> and MgO in their respective ratios. The precursors were mixed with SPEX 8000 M MIXER/MILL using two 20 mm stainless steel balls (30 g) for 1.5 h. The mixture was then heated at 900 °C for 12 h in air and slowly cooled down to room temperature.

**Electrochemical characterization.** For the electrochemical analysis, the electrodes were prepared by mixing the active material with conductive carbon (Super P) and polyvinylidene fluoride (PVdF Kynar Flex) as binder in a ratio of 8:1:1, respectively. A few drops of *N*-methyl-2-pyrrolidone (NMP) (Sigma Aldrich) was added to the slurry mixture and ball-milled at 600 rpm for 2 h. The slurry was then casted on carbon coated Al-foil by the doctor-blade technique, dried at 80 °C and then

punched into 13 mm diameter electrode discs. The electrodes were then introduced into an argon-filled glovebox (H<sub>2</sub>O < 2 ppm and O<sub>2</sub> < 3 ppm) and then dried under vacuum at 120 °C for 12 h to remove residues of solvent and moisture. The half-cells were assembled in polyethylene-coated aluminium pouch cells, in which Na-metal (Sigma Aldrich) on Al-foil was used as counter electrode with Solupor<sup>®</sup> as the separator, Al as current collectors and 1 M NaPF<sub>6</sub> (Stella) in PC (BASF) as the electrolyte. The whole assembly was conducted in an argon-filled glovebox (H<sub>2</sub>O < 2 ppm and O<sub>2</sub> < 3 ppm). The assembled cells were then cycled galvanostatically with a Digatron BTS 600 instrument. The cycling was conducted in a voltage window of 2.0–4.5 V for 20 cycles at 0.1 C in room temperature. The 0.1 C-rate here is assumed for 10 h charge or discharge, hence desodiation or sodiation.

Cyclic voltammetry measurements were performed with a Bio-Logic VMP2 instrument. The cells were cycled for 10 cycles in a voltage window of 2.0–4.5 V at a scan rate of 0.1 mV s<sup>-1</sup>.

**ICP-OES.** The chemical composition of the compound was determined via ICP-OES by using the instrument Avio 200.

**In situ XRD.** XRD patterns of the pristine powder and the in situ analysis were recorded on a Stoe & Cie GmbH Stadi X-ray powder diffractometer equipped with a Ge monochromator (Cu K<sub>α1</sub>) using transmission mode. The detector at Mythen 1k Si strip detector operated in a sweeping mode with a resolution of 0.015° 2θ.

**XAS and RIXS.** Soft XAS over the O K-edge and the TM L-edges and RIXS over the O K-edge were performed at beamline 8.0.1 of the Advanced Light Source (ALS) of Lawrence Berkeley National Laboratory (LBNL). The undulator beamline is equipped with a spherical grating monochromator. The approximately 100 nm bulk-sensitive TFY XAS spectra were collected with a Channeltron electron multiplier with negative bias to reject photoelectrons. Additionally, up to 10 nm and therefore more surface-sensitive TEY was recorded as the drain current back into the sample via a nanoammeter. For both modes the monochromator band width varied between 0.1 and 0.2 eV, depending on incident energy. The O K-edge RIXS measurements were taken using a high-resolution Rowland circle type grating spectrometer<sup>56</sup>. The combined instrumental (monochromator and spectrometer) resolution was 0.3 eV. By integrating over the O RIXS peak the partial fluorescence yield (PFY) was determined as an additional bulk-sensitive signal which is intrinsically free from any possible influence of photoelectrons.

Following the established procedure<sup>36</sup>, all XAS spectra have been normalized by the incident intensity *I*<sub>0</sub> determined by the beam flux, which was measured as drain current from an upstream Au-coated mesh. Lines were fitted to the (mostly) flat regions below any absorption peaks and subsequently subtracted from each whole spectrum in order to clear it from a sloping, linear background. Further normalization was done by setting the low-energy region before any absorption peaks to zero and the post-edge region after any absorption features to unity. In the case of O K-edge XAS the low-intensity region directly after the pre-edge features, at 533.5 eV was set to unity.

**PES.** Energy-tuned PES analysis of the material surface and bulk was performed at the beamline (I09) at Diamond Light Source (Oxfordshire, UK). The tested electrodes were fixed via copper tape on a copper plate at the end-station at the synchrotron.

HAXPES measurements with excitation energies of 2350 and 7050 eV were made using an Si(111) double-crystal monochromator, whereas SOXPES was performed by using excitation energy of 1090 eV at a branch of the beamline with a plane grating monochromator. In order to minimize radiation damage, the beam was dispersed via using defocused settings. The measured sample spot is ca. 300 μm long and up to 1 mm wide. During the measurements no charge neutralizer was

used. To record the spectra a hemispherical VG Scienta EW4000 analyser which is set to a pass energy of 50 eV for soft X-rays and 200 eV for hard X-rays was utilized. The data analysis of the PES spectra was conducted using Igor Pro. To calibrate the binding energies in the recorded spectra the peak originated from the carbon black in the electrodes set at 285 eV in the C 1s spectra was used.

### Data availability

The data that support the plots with this paper and other finding of this study are available from the corresponding author upon reasonable request.

Received: 26 April 2019; Accepted: 14 October 2019;

Published online: 06 November 2019

### References

- Tarascon, J.-M. Is lithium the new gold? *Nat. Chem.* **2**, 510–510 (2010).
- Roberts, S. & Kendrick, E. Nanotechnology, science and applications Dovepress: the re-emergence of sodium ion batteries: testing, processing, and manufacturability. *Nanotechnol. Sci. Appl.* **11**, 11–23 (2018).
- Pan, H., Hu, Y.-S. & Chen, L. Room-temperature stationary sodium-ion batteries for large-scale electric energy storage. *Energy Environ. Sci.* **6**, 2338–2360 (2013).
- Dahbi, M., Yoshida, H., Kubota, K., Komaba, S. & Yabuuchi, N. Layered oxides as positive electrode materials for Na-ion batteries. *MRS Bull.* **39**, 416–422 (2014).
- Sanz, F., Parada, C., Rojo, J. M. & Ruiz-Valero, C. Crystal structure, magnetic properties, and ionic conductivity of a new mixed-anion phosphate  $\text{Na}_4\text{Ni}_5(\text{PO}_4)_2(\text{P}_2\text{O}_7)_2$ . *Chem. Mater.* **11**, 2673–2679 (1999).
- Wang, L. A superior low-cost cathode for a Na-Ion battery. *Angew. Chem. Int. Ed.* **52**, 1964–1967 (2013).
- Brant, W. R. et al. Selective control of composition in Prussian white for enhanced material properties. *Chem. Mater.* **31**, 7203–7211 (2019).
- Valvo, M., Doubaji, S., Saadoun, I. & Edström, K. Pseudocapacitive charge storage properties of  $\text{Na}_{2/3}\text{Co}_{2/3}\text{Mn}_{2/9}\text{Ni}_{1/9}\text{O}_2$  in Na-ion batteries. *Electrochim. Acta* **276**, 142–152 (2018).
- Delmas, C., Fouassier, C. & Hagemuller, P. Structural classification and properties of the layered oxides. *Physica B+C* **99**, 81–85 (1980).
- Nakai, I. et al. Study on the reversible electrode reaction of  $\text{Na } 1-x \text{ Ni } 0.5\text{Mn } 0.5\text{O}_2$  for a rechargeable sodium-ion battery. *Inorg. Chem.* **51**, 6211–6220 (2012).
- Slater, M. D., Kim, D., Lee, E. & Johnson, C.S. Sodium-ion batteries. *Adv. Funct. Mater.* **23**, 947–958 (2013).
- Lu, Z. & Dahn, J. R. In situ X-ray diffraction study of  $\text{P2-Na}_{2/3}[\text{Ni}_{1/3}\text{Mn}_{2/3}]\text{O}_2$ . *J. Electrochem. Soc.* **148**, A1225 (2001).
- Lee, D. H., Xu, J. & Meng, Y. S. An advanced cathode for Na-ion batteries with high rate and excellent structural stability. *Phys. Chem. Chem. Phys.* **15**, 3304–3312 (2013).
- Hasa, I., Passerini, S. & Hassoun, J. Toward high energy density cathode materials for sodium-ion batteries: investigating the beneficial effect of aluminum doping on the P2-type structure. *J. Mater. Chem. A* **5**, 4467–4477 (2017).
- Singh, G. et al. High voltage Mg-doped  $\text{Na}_{0.67}\text{Ni}_{0.3-x}\text{Mg}_x\text{Mn}_{0.7}\text{O}_2$  ( $x=0.05, 0.1$ ) Na-ion cathodes with enhanced stability and rate capability. *Chem. Mater.* **28**, 5087–5094 (2016).
- Zhao, W. et al. Synthesis of metal ion substituted  $\text{P2-Na}_{2/3}\text{Ni}_{1/3}\text{Mn}_{2/3}\text{O}_2$  cathode material with enhanced performance for Na ion batteries. *Mater. Lett.* **135**, 131–134 (2014).
- Hemalatha, K., Jayakumar, M., Bera, P. & Prakash, A. S. Improved electrochemical performance of  $\text{Na}_{0.67}\text{MnO}_2$  through Ni and Mg substitution. *J. Mater. Chem. A* **3**, 20908–20912 (2015).
- Li, Z. Y. et al. New insights into designing high-rate performance cathode materials for sodium ion batteries by enlarging the slab-spacing of the Na-ion diffusion layer. *J. Mater. Chem. A* **4**, 3453–3461 (2016).
- Wang, P. F. Suppressing the P2-O2 phase transition of  $\text{Na}_{0.67}\text{Mn}_{0.67}\text{Ni}_{0.33}\text{O}_2$  by magnesium substitution for improved sodium-ion batteries. *Angew. Chem. Int. Ed.* **55**, 7445–7449 (2016).
- Li, B. et al. Review on anionic redox for high-capacity lithium- and sodium-ion batteries. *J. Phys. D Appl. Phys.* **50**, 183001 (2017).
- Luo, K. et al. Anion redox chemistry in the cobalt free 3d transition metal oxide intercalation electrode  $\text{Li}[\text{Li}_{0.2}\text{Ni}_{0.2}\text{Mn}_{0.6}]\text{O}_2$ . *J. Am. Chem. Soc.* **138**, 11211–11218 (2016).
- Lefief, C. et al. The significance of the  $\text{Li}_2\text{MnO}_3$  component in ‘composite’  $x\text{Li}_2\text{MnO}_3\text{-(1-x)}\text{LiMn}_{0.5}\text{Ni}_{0.5}\text{O}_2$  electrodes. *Electrochem. Commun.* **6**, 1085–1091 (2004).
- Rossouw, M. et al. Structural aspects of lithium-manganese-oxide electrodes for rechargeable lithium batteries. *Mater. Res. Bull.* **25**, 173–182 (1990).
- Robertson, A. D. & Bruce, P. G. Mechanism of electrochemical activity in  $\text{Li}_2\text{MnO}_3$ . *Chem. Mater.* **15**, 1984–1992 (2003).
- Yu, D. Y. W., Yanagida, K., Kato, Y. & Nakamura, H. Electrochemical activities in  $\text{Li}_2\text{MnO}_3$ . *J. Electrochem. Soc.* **156**, A417 (2009).
- Francis Amalraj, S. et al. Study of the electrochemical behavior of the ‘inactive’  $\text{Li}_2\text{MnO}_3$ . *Electrochim. Acta* **78**, 32–39 (2012).
- Robertson, A. D. & Bruce, P. G. The origin of electrochemical activity in  $\text{Li}_2\text{MnO}_3$ . *Chem. Commun.* **23**, 2790–2791 (2002).
- Park, J.-H. et al. Continuous activation of  $\text{Li}_2\text{MnO}_3$  component upon cycling in  $\text{Li}_{1.167}\text{Ni}_{0.233}\text{Co}_{0.100}\text{Mn}_{0.467}\text{Mo}_{0.033}\text{O}_2$  cathode material for lithium ion batteries. *J. Mater. Chem. A* **1**, 2833 (2012).
- Carlier, D. et al. The  $\text{P2-Na}_{2/3}\text{Co}_{2/3}\text{Mn}_{1/3}\text{O}_2$  phase: structure, physical properties and electrochemical behavior as positive electrode in sodium battery. *Dalton Trans.* **40**, 9306–9312 (2011).
- Zhou, T., Zhang, D., Button, T. W., Wright, A. J. & Greaves, C. Influence of cooling rate on the structure and composition of  $\text{Na}_x\text{CoO}_2$  ( $x\sim 0.65$ ). *J. Mater. Chem.* **19**, 1123–1128 (2009).
- Sathiyaa, M., Hemalatha, K., Ramesha, K., Tarascon, J.-M. M. & Prakash, A. S. Synthesis, structure, and electrochemical properties of the layered sodium insertion cathode material:  $\text{NaNi}_{1/3}\text{Mn}_{1/3}\text{Co}_{1/3}\text{O}_2$ . *Chem. Mater.* **24**, 1846–1853 (2012).
- Palanisamy, M., Kim, H. W., Heo, S., Lee, E. & Kim, Y. Insights into the dual-electrode characteristics of layered  $\text{Na}_{0.5}\text{Ni}_{0.25}\text{Mn}_{0.75}\text{O}_2$  materials for sodium-ion batteries. *ACS Appl. Mater. Interfaces* **9**, 10618–10625 (2017).
- Buchholz, D. et al. Toward na-ion batteries—synthesis and characterization of a novel high capacity na ion intercalation material. *Chem. Mater.* **25**, 142–148 (2013).
- Hasa, I., Buchholz, D., Passerini, S. & Hassoun, J. A comparative study of layered transition metal oxide cathodes for application in sodium-ion battery. *ACS Appl. Mater. Interfaces* **7**, 5206–5212 (2015).
- Hasa, I., Buchholz, D., Passerini, S., Scrosati, B. & Hassoun, J. High performance  $\text{Na}_{0.5}[\text{Ni}_{0.23}\text{Fe}_{0.13}\text{Mn}_{0.63}]\text{O}_2$  cathode for sodium-ion batteries. *Adv. Energy Mater.* **4**, 1400083 (2014).
- Stöhr, J. *NEXAFS Spectroscopy* (Springer, 1992).
- Henderson, G. S., de Groot, F. M. F. & Moulton, B. J. A. X-ray absorption near-edge structure (XANES). *Spectrosc. Rev. Mineral. Geochem.* **78**, 75–138 (2014).
- De Groot, F. M. F. X-ray absorption and dichroism of transition metals and their compounds. *J. Electron Spectros. Relat. Phenom.* **67**, 529–622 (1994).
- Abbate, M. et al. Probing depth of soft x-ray absorption spectroscopy measured in total-electron-yield mode. *Surf. Interface Anal.* **18**, 65–69 (1992).
- Ashley, J. C. Energy losses and inelastic mean free paths of low-energy electrons in polyethylene. *Radiat. Res.* **90**, 433 (2006).
- Seah, M. P. The quantitative analysis of surfaces by XPS: a review. *Surf. Interface Anal.* **2**, 222–239 (1980).
- Qiao, R., Chin, T., Harris, S. J., Yan, S. & Yang, W. Spectroscopic fingerprints of valence and spin states in manganese oxides and fluorides. *Curr. Appl. Phys.* **13**, 544–548 (2013).
- Tröger, L. et al. Full correction of the self-absorption in soft-fluorescence extended x-ray-absorption fine structure. *Phys. Rev. B* **46**, 3283–3289 (1992).
- Eisebitt, S., Boske, T., Rubensson, J.-E. & W., E. Determination of absorption coefficients for concentrated samples by fluorescence detection. *Phys. Rev. B* **47**, 103–109 (1993).
- de Groot, F. M. F. Differences between L3 and L2 X-ray absorption spectra. *Phys. B Condens. Matter* **208–209**, 15–18 (1995).
- Ilton, E. S., Post, J. E., Heaney, P. J., Ling, F. T. & Kerisit, S. N. XPS determination of Mn oxidation states in Mn (hydr)oxides. *Appl. Surf. Sci.* **366**, 475–485 (2016).
- Trotsenko, V. G. et al. Valence state of manganese and iron ions in  $\text{La}_{1-x}\text{A}_x\text{MnO}_3$  ( $\text{A} = \text{Ca, Sr}$ ) and  $\text{Bi}_{1-x}\text{Sr}_x\text{FeO}_3$  systems from Mn2p, Mn3s, Fe2p and Fe3s X-ray photoelectron spectra. Effect of delocalization on Fe3s spectra splitting. *J. Alloy. Compd.* **647**, 947–955 (2015).
- Galakhov, V. R. et al. Mn 3s exchange splitting in mixed-valence manganites. *Phys. Rev. B* **65**, 113102 (2002).
- Lau, L. W. M. et al. Resolving surface chemical states in XPS analysis of first row transition metals, oxides and hydroxides: Cr, Mn, Fe, Co and Ni. *Appl. Surf. Sci.* **257**, 2717–2730 (2010).
- Wang, H. et al. Integrated X-ray L3 Absorption Spectra. Counting Holes in Ni Complexes. *J. Phys. Chem. B* **102**, 8343–8346 (1998).
- De Groot, F. M. F. et al. Oxygen 1s X-ray-absorption edges of transition-metal oxides. *Phys. Rev. B* **40**, 5715–5723 (1989).
- Liu, Y.-S. et al. Charge-compensation in 3d-transition-metal-oxide intercalation cathodes through the generation of localized electron holes on oxygen. *Nat. Chem.* **8**, 684–691 (2016).
- Maitra, U. et al. Oxygen redox chemistry without excess alkali-metal ions in  $\text{Na}_{2/3}[\text{Mg}_{0.28}\text{Mn}_{0.72}]\text{O}_2$ . *Nat. Chem.* **10**, 288–295 (2018).
- Ma, C. et al. Exploring oxygen activity in the high energy P2-type  $\text{Na}_{0.78}\text{Ni}_{0.23}\text{Mn}_{0.69}\text{O}_2$  cathode material for Na-ion batteries. *J. Am. Chem. Soc.* **139**, 4835–4845 (2017).



55. Carniato, S. et al. A new method to derive electronegativity from resonant inelastic x-ray scattering. *J. Chem. Phys.* **137**, 144303 (2012).
56. Qiao, R. et al. High-efficiency in situ resonant inelastic x-ray scattering (iRIXS) endstation at the Advanced Light Source. *Rev. Sci. Instrum.* **88**, 033106 (2017).

### Acknowledgements

The work was supported by the Department of Chemistry-Ångström Laboratory and the Department of Physics at Uppsala University. The research has also been supported by the project CALIPSOplus under the Grant Agreement 730872 from the EU Framework Programme for Research and Innovation HORIZON 2020. This work was carried out with the support of the Diamond Light Source (Oxfordshire, UK), instrument I09 (proposal SI18974-1). This research also used resources of Advanced Light Source (ALS) of Lawrence Berkeley National Laboratory (LBNL) at beamline 8.0.1 which is a DOE Office of Science User Facility under contract no. DE-AC02-05CH11231 with Yi-Sheng Liu as the beamline scientist and Jinghua Guo as the corresponding beamline manager. L.A.M. and R.Y. acknowledge funding from the Swedish Research Council for Environment, Agricultural Sciences and Spatial Planning (Formas) via the grant 2016-01257 and from STandUP for Energy. Open access funding provided by Uppsala University.

### Author contributions

L.A.M. and R.Y. designed the experiments. L.A.M. performed synthesis, XRD, ICP-OES and electrochemical measurements. L.A.M. collected and analysed the PES data with assistance from A.J.N. F.M. collected and analysed the XAS and RIXS data with assistance of L.D. L.A.M. and R.Y. participated in the XAS and RIXS data discussion. L.A.M. analysed the data and wrote the manuscript with the help of all coauthors. R.Y. lead the project.

### Competing interests

The authors declare no competing interests.

### Additional information

Supplementary information is available for this paper at <https://doi.org/10.1038/s42004-019-0227-z>.

Correspondence and requests for materials should be addressed to R.Y.

Reprints and permission information is available at <http://www.nature.com/reprints>

**Publisher's note** Springer Nature remains neutral with regard to jurisdictional claims in published maps and institutional affiliations.



**Open Access** This article is licensed under a Creative Commons Attribution 4.0 International License, which permits use, sharing, adaptation, distribution and reproduction in any medium or format, as long as you give appropriate credit to the original author(s) and the source, provide a link to the Creative Commons license, and indicate if changes were made. The images or other third party material in this article are included in the article's Creative Commons license, unless indicated otherwise in a credit line to the material. If material is not included in the article's Creative Commons license and your intended use is not permitted by statutory regulation or exceeds the permitted use, you will need to obtain permission directly from the copyright holder. To view a copy of this license, visit <http://creativecommons.org/licenses/by/4.0/>.

© The Author(s) 2019